RESEARCH ARTICLE

National Science Open
4: 20240022, 2025
https://doi.org/10.1360/nso/20240022

Earth and Environmental Sciences

Spreading of marine radionuclides through sea spray

Yaru Song, Kun Li, Jianlong Li, Narcisse Tsona Tchinda & Lin Du*

Qingdao Key Laboratory for Prevention and Control of Atmospheric Pollution in Coastal Cities, Environment Research Institute, Shandong University, Qingdao 266237, China

*Corresponding author (email: lindu@sdu.edu.cn)

Received 29 May 2024; Revised 30 December 2024; Accepted 7 January 2025; Published online 9 January 2025

Abstract: In August 2023, a significant release of radionuclides occurred from the Fukushima Daiichi nuclear power plants, dispersing into the western Pacific Ocean. Sea spray aerosols (SSA) were identified as an important pathway for their atmospheric transport. In this study, an SSA simulation chamber was employed to investigate the enrichment and transport behavior of SSA generated from seawater containing nine different metal ions (Co^{2+}, Ba^{2+}, Mn^{2+}, Sb^{3+}, Cs^{+}, Sr^{2+}, Rh^{3+}, La^{3+}, and Ru^{3+}). Radionuclides showed consistent enrichment with Ca^{2+}, Mg^{2+}, and K^{+}, confirming SSA-mediated transport into the atmosphere. Additionally, the enrichment factor analysis suggested that marine organic matter could enhance the atmospheric emission of metal ions. Trajectory simulations further demonstrated that radionuclide-enriched SSAs can travel long distances, contributing to atmospheric deposition in both marine and terrestrial environments. This study combines experimental and modelling approaches to reveal radionuclides transport via SSAs and provides insights into their environmental impact.

Keywords: sea spray aerosols, radionuclides, particle size distribution, enrichment factor

INTRODUCTION

The Fukushima Daiichi nuclear power plants (FDNPPs) discharged a substantial quantity of radionuclides into the ocean on August 24, 2023. This has become a matter of great concern raising questions about the fate and impact of these radionuclides on the marine ecosystem [1–7]. In recent years, the direct discharge of radionuclides from nuclear accidents into the ocean has led to severe pollution, posing significant environmental and health risks [8,9]. These incidents have raised concerns globally due to their potential long-term impacts on marine ecosystems and human populations [10–12]. Among these accidents, large quantities of radionuclides enter the ocean directly, and the radionuclides affect the entire northern hemisphere and even parts of the southern hemisphere [11,13]. Due to the complexity of monitoring the ocean, relatively few studies have performed comparative analysis of marine emissions and atmospheric emissions.

As early as 2011, the severe accident that occurred at the FDNPP following a massive earthquake and tsunami was classified as a Level 7 event, the highest level on the international nuclear accident scale, by the International Atomic Energy Agency [14,15]. As a result of this incident, Japan was mandated to establish and operate environmental radioactivity monitoring systems at nuclear power plants [16]. Over the past thirteen years, substantial data from numerous studies on this accident have gradually been compiled into

© The Author(s) 2025. Published by Science Press and EDP Sciences. This is an Open Access article distributed under the terms of the Creative Commons Attribution License (https://creativecommons.org/licenses/by/4.0), which permits unrestricted use, distribution, and reproduction in any medium, provided the original work is properly cited.

international literature [8,17–26]. Not only have changes in atmospheric radioactivity levels been monitored, but the transport pathways of atmospheric radionuclides have also been extensively modeled [27–35]. While land and atmospheric radioactivity levels of discharged radionuclides have been monitored, and although the transport of radionuclides through the atmosphere and oceans has been modeled and predicted, few studies of radioactivity in the marine environment have been reported [25]. The quantities of radionuclides discharged into the ocean were substantial, primarily affecting the Pacific Ocean. The level of radioactivity in the ocean around the site of the nuclear accident rapidly increased within a short time. Therefore, it is extremely urgent to take measures to monitor and manage areas with high radioactivity caused by nuclear accidents.

Besides the concerns about increasing levels of radioactivity in the ocean, research on radionuclides entering the oceans so far has mainly focused on their transport mechanisms and pathways [11]. One significant pathway through which radioactive elements are transported is via sea spray aerosols (SSAs), which are generated at the air-sea interface [36]. The SSAs can carry a wide range of substances including salts, organic matter, microorganisms, and trace elements [37]. Moreover, these components can exhibit varying degrees of enrichment or depletion within SSA, significantly influencing its properties and further impacting the climate [38–41]. These aerosol particles may also carry radionuclides over long distances, affecting not only local marine ecosystems but also regions far from the source of contamination. Understanding the mechanisms and dynamics of radionuclides transport process via SSAs is crucial for accurate risk assessment and mitigation strategies. Forward and backward air mass trajectory simulations are of critical importance in tracing the pathways of these particles [42]. Forward trajectories assist in identifying the transport routes of radionuclides that are enriched in SSA particles from their source regions, while backward trajectories facilitate the determination of potential source areas for radionuclides observed in specific locations [43,44]. This dual approach provides indispensable insights into how radionuclides, once incorporated into SSA particles, are transported via atmospheric pathways, thereby amplifying their environmental impact.

Furthermore, considering that the presence of organic components in seawater may influence the transport behavior of radionuclides, organic matter may act as carriers or sorbents, thereby affecting the mobility and bioavailability of radionuclides in the marine environment. Investigating the interactions between organic compounds and radionuclides is essential for a comprehensive assessment of the fate and potential impacts of nuclear contamination in the ocean.

The current research builds upon our custom-made SSA simulation chamber, proposing a potential transport pathway of radionuclides and has two primary objectives. The first objective is to explore the transport process of radionuclides through SSA, while simultaneously analyzing the concentration of radionuclides in both seawater and SSA samples, and subsequently calculating their enrichment factors (EFs) thereafter. The second objective is to investigate the impact of organic components in seawater on the enrichment behavior of radionuclides. Given that this study focuses on chemical enrichment and partitioning behavior, which is mainly driven by ionic interactions and adsorption processes [45], using non-radioactive metals as proxies provides valid and reliable insights into the behavior of radionuclides. By integrating the experimental data, unique insights into the enrichment behavior of radionuclides at the sea-air interface are expected to be obtained. By combining experimental data and trajectory modelling, this study aims to provide complementary insights into the enrichment mechanisms of radionuclides at the air-sea interface and the transport dynamics of SSA particles to the atmosphere.

MATERIALS AND METHODS

Materials

Standard solutions of radionuclides were purchased from Beijing Mreda Technology. Nine radionuclides including ions of cobalt (Co^{2+}), barium (Ba^{2+}), manganese (Mn^{2+}), antimony (Sb^{3+}), cesium (Cs^{+}), strontium (Sr^{2+}), rhodium (Rh^{3+}), lanthanum (La^{3+}), and ruthenium (Ru^{3+}) were investigated. Formic acid, hexanoic acid, octanoic acid, and phthalic acid were purchased from Shanghai Aladdin Bio-Chem Technology, and they were investigated as model materials of marine organic matter to determine the influence of chain length and molecular structure on metal ions at the sea-air interface. The nitric acid solution was provided by China National Pharmaceutical Group Chemical Reagent. Seawater was collected from the remote western Pacific Ocean using a centrifugal pump and stored in precleaned plastic bottles. The pH values, measured using a pH meter (PHS-3C, Shanghai Yidian Scientific Instrument, China), ranged from 7.58 to 7.92 across all experiments involving radionuclides and marine organic matter, while the natural seawater pH ranges from 7.90 to 8.17. Ultrapure water, with a resistivity of 18.2 MΩ cm, was produced utilizing a Milli-Q purification system (Merck Millipore, France), suitable for preparing mobile phases for liquid chromatography. The summary of the concentrations of radionuclides in seawater and SSA samples, as well as the ionic strength in seawater, are provided in Tables S1, S2, and S3 in the Supplementary information.

Experimental setup

A jet-based laboratory simulation chamber was employed to simulate the generation of SSAs [40,46–48], as depicted in Figure S1. This chamber, a clamshell cuboid box measuring 30 cm in length, 20 cm in width, and 40 cm in height, featured a viewable glass window and has been recently modified for studies on air-sea transport processes. It utilized continuously generated plunging jets to produce realistic SSA. All enrichment experiments were conducted within this simulation chamber, which was filled with approximately 9 L of seawater. Plunging jets were activated in the seawater by a pump at a flow rate of 1 L min^{-1} through a stainless-steel nozzle. Bubble breaking at the seawater surface was observed through the attached glass window. To prevent contamination from indoor air, particle-free air was supplied by a compressor and zero-air generator (model 111, Thermo Scientific, USA). A mass flow controller (Beijing Sevenstar Electronics, China) regulated the airflow rate into the simulation chamber, ranging from 3 to 50 L min^{-1}. The relative humidity of the aerosol at the sampling port was controlled using a Nafion drying tube (MD-700-06S-3, Perma Pure, USA). Relative humidity and temperature were monitored by a 2-channel thermo-hygrometer (Testo HM42, Vaisala, Finland), maintained within the ranges of 30%–40% and 20–25 °C, respectively. The surface tension of 30 mL seawater samples was measured using a tensiometer (JK99C, Powereach, China), which was calibrated with ultrapure water at 25 °C. Calibration was performed once every three measurements. The platinum plate was cleaned with ethanol before each measurement.

Sample collection and instrumental analysis

The particle size distributions were assessed under a relative humidity of approximately 30% using a

scanning mobility particle sizer (SMPS, TSI, Model 3936). SSA particles are charged within the differential mobility analyzer (DMA, Model 3081, TSI, USA), where particles of different sizes and charges are separated and focused into distinct size bins. Subsequently, these particles enter the condensation particle counter (CPC, Model 3776, TSI, USA), which detects and counts the particles in each size bin, providing information about the particle size distribution with diameters ranging from 14.1 to 710.5 nm. Within the SSA simulation chamber, the SMPS monitored the number concentration and geometric mean diameter (GMD) of particles at intervals of 3 min. The inlet and sheath gas flow rates were set at 0.3 and 3.0 L min^{-1}, respectively. Prior to activating the pump, it was ensured that the particle number concentration remained below 20 particles cm^{-3} for the initial 30 min of each experiment, confirming the absence of leaks and background particles. Each set of experiments for monitoring number concentration lasted approximately 1 h. The particle size distribution of SSA in our experiment, consistent with general trends observed in field measurements (Figure S2) [49,50], was achieved by carefully controlling key parameters such as the inner diameter of the stainless steel nozzle, headspace height, pump flow rates, and purge air flow rates [46].

A flow of zero air at a rate of 10 L min^{-1} passed over the sea surface within a chamber, carrying SSA particles through a Nafion drying tube (MD-700-06S-3, Perma Pure, USA) to a 47 mm quartz fiber filter (QFF, 1851-025, Waterman, UK) for the collection of total particulate matter. SSA particles were impacted onto a QFF with a diameter of 25 mm, and subsequently baked in a muffle furnace at 450 °C for 3 h. The low-pressure impactor collected submicron samples in stages 6–10 (0.19–0.94 μm) and supermicron samples in stages 11–15 (1.62–10 μm).

Filters were extracted in 4 mL of ultrapure water under ultrasonic conditions for 30 min. Nitric acid was added to the samples to achieve a concentration of 2% HNO_3 in each sample. All samples were analyzed using an inductively coupled plasma mass spectrometry (ICP-MS) instrument (NexION 1000G, PerkinElmer, Singapore). Sample solutions were introduced into the mass spectrometer via a peristaltic pump. The nebulizer in the sample introduction system was a Meinhard glass concentric nebulizer, with a cyclonic spray chamber. The interface employed was the PerkinElmer three-cone system, consisting of nickel skimmer cone, sampler cone, and hyper skimmer cone, with diameters of 1.1, 0.9 and 1.0 mm, respectively. The design of the three cones not only reduced blockage of the cone orifice by complex samples but also minimized contamination of lenses and mass analyzers. The instrument was equipped with a reaction cell, allowing detection in three modes: standard, collision, and reaction mode, with rapid mode switching between them. Specific instrument parameters used in the experiments, aside from the default values of the instrument itself, are detailed in Table S4.

Inorganic ions in seawater and SSA samples were filtered through a 0.22 μm PTFE filter and analyzed using ion chromatography (Dionex ICS-6000, Thermo Fisher Scientific, USA) coupled with conductivity detection. Cations were separated on a Dionex IonPac CS12A (4 mm × 250 mm) column with a pre-column guard and eluted with 20 mM methanesulfonic acid at a flow rate of 1 mL min^{-1}. The injection volume was 10 μL for each sample.

The EF of metal ions was then calculated using Eq. (1),

$$EF = \frac{[X]_{SSA} / [Na^+]_{SSA}}{[X]_{SW} / [Na^+]_{SW}}, \quad (1)$$

where $[X]_{SSA}$ and $[Na^+]_{SSA}$ are the concentrations of metal ions and Na^+ in SSA, $[X]_{SW}$ and $[Na^+]_{SW}$ denote respective concentrations in seawater [51].

Forward and backward trajectory calculations

The meteorological fields input for the Hybrid Single Particle Lagrangian lntegrated Trajectory (HYSPLIT) model is sourced from the Global Data Assimilation System (GDAS) by NOAA, with a spatial resolution of 1°×1° and a temporal resolution that can reach hourly intervals. In this study, forward and backward trajectories for every hour up to 48 h are computed for the research locations. Cluster analysis is primarily employed throughout the study to analyze the data comprehensively. The simulated air masses represent the trajectories of SSA particles carried by atmospheric flows.

The forward trajectories were initiated from FDNPP (141.20°E, 37.25°N), assuming that the particles remained at approximately the same pressure levels throughout their transport. In contrast, the backward trajectories arriving in Qingdao (120.41°E, 36.08°N) were simulated in a direction opposite that of the forward trajectories. The model was run twice per day, at 00:00 and 18:00 UTC. To focus on the marine environment, the trajectory simulations were set at 100 m above ground level (AGL), representing the atmospheric boundary layer over the ocean. This height was selected to capture the transport of pollutants near the air-sea interface, where interactions between the atmosphere and ocean are most significant [52–57].

Cluster analysis, conducted using the TrajStat in MeteoInfo software, was applied to group similar trajectories based on their spatial and temporal characteristics [58–61]. This process involved normalizing trajectory coordinates to a standard grid and calculating the Euclidean distances between trajectories to quantify their similarity. Using hierarchical clustering algorithms, trajectories were grouped into clusters with similar pathways, with each cluster represented by a centroid trajectory. This approach allowed for a comprehensive analysis of transport pathways, effectively identifying common atmospheric transport routes and regions where pollutants may accumulate or disperse. The clustering analysis provided valuable insights into the transport mechanisms of radionuclides and SSA particles over the marine environment, revealing how pollutant enrichment and dispersion patterns are influenced by atmospheric dynamics.

RESULTS

SSA size distribution containing radionuclides

The influence of radionuclides on SSA generation was studied by measuring the particle size distribution of SSA generated in the simulation chamber. Figure 1A shows the particle size distribution of sea salt particles and particles with added radionuclides. Initially, the number concentration of SSA particles generated from seawater was tested, and upon stabilization, it was found that the peak number concentration was around 182.26 nm, which could be fitted to a log-normal distribution observed in previous studies [49,50,62].

After the SSA number size distribution was stabilized, the metal ions were added. The number concentration of the SSA particles decreased slightly from 2.22×10^4 to 2.07×10^4 particles cm^{-3} during the experiment (Figure S3), which is within the acceptable range of our experimental setup. The number concentration of SSA particles was significantly higher than that of sea salt particles following the addition of metal ions, and an increase in bubble bursting could be visually observed through the window of the SSA simulation chamber. As shown in Figure 1B, the surface tension of seawater increased after the addition of metal ions. The observed bursting phenomenon is consistent with the conclusion that high seawater surface

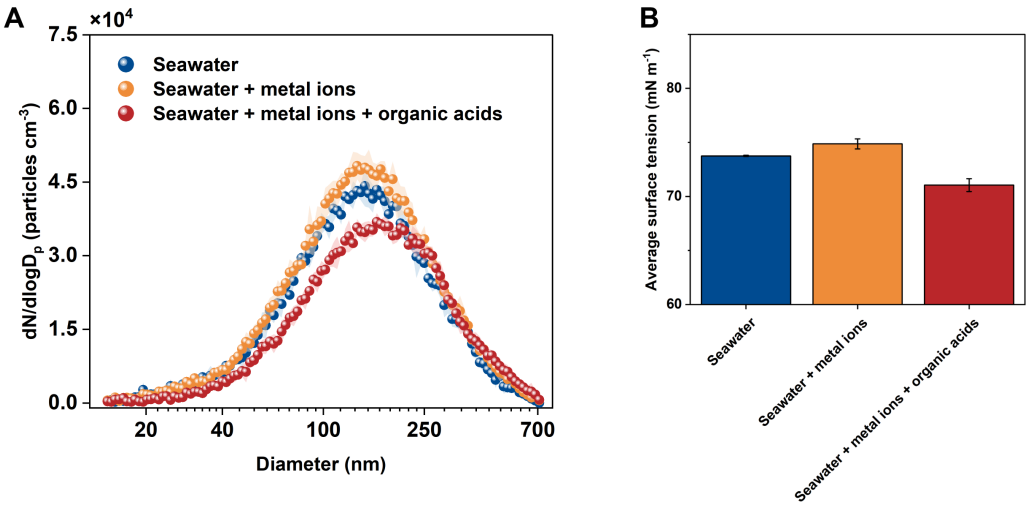


Figure 1 (A) The number concentration distribution of sea salt particles and SSA particles containing metal ions and marine organic matter. (B) Measured surface tension values of natural seawater.

tension can promote SSA production [46,63]. After the addition of marine organic matter to the system, the number concentration of SSA particles decreased noticeably. Concurrently, the surface tension of seawater decreased as well. This indicates that the addition of marine organic matter, acting as surfactants, enhanced the surface activity of seawater.

In terms of particle size distribution, the wider particle size distribution and slightly larger particle diameters observed in the system with added metal ions compared to sea salt particles indicate that metal ions play a significant role in promoting the formation of SSA particles. After adding marine organic matter to the bulk water containing metal ions, the number concentration of SSA particles significantly decreased, indicating that the addition of marine organic matter inhibited SSA production. This is consistent with previous findings showing that the addition of marine organic matter inhibits the generation of SSA particles [40]. Moreover, considering the mode diameter of SSA particles, the addition of marine organic matter noticeably increased the particle size of SSA. The composition of radionuclides may be influenced by factors such as ionic strength, surfactants, and ion adsorption at the liquid surface, which could affect the surface tension values [63–66].

Enrichment behavior of radionuclides to SSA particles

Aerosolization was estimated to be the main reason for the decrease in concentration of radionuclides in SSA particles, with the extent of the reduction variation depending on the species of radionuclides. By characterizing the EFs of various metal ions in SSA, the influence of different metal ions on the accumulation of SSA from seawater to the atmosphere was visually demonstrated. As shown in Figure 2A, all metal ions exhibited varying degrees of EFs in SSA particles, except the EFs of La^{3+} and Ru^{3+} less than 1, indicating depletion. The EFs ranged from 0.28 to 2.49, with the largest and smallest being those of Co^{2+} and Ru^{3+}, respectively. Co^{2+}, Ba^{2+}, and Mn^{2+} belong to a category of highly enriched metal ions ($1.5 < EF < 3$), and they exhibit enrichment characteristics similar to Ca^{2+} in seawater. As mentioned in previous studies, Ca^{2+} not only

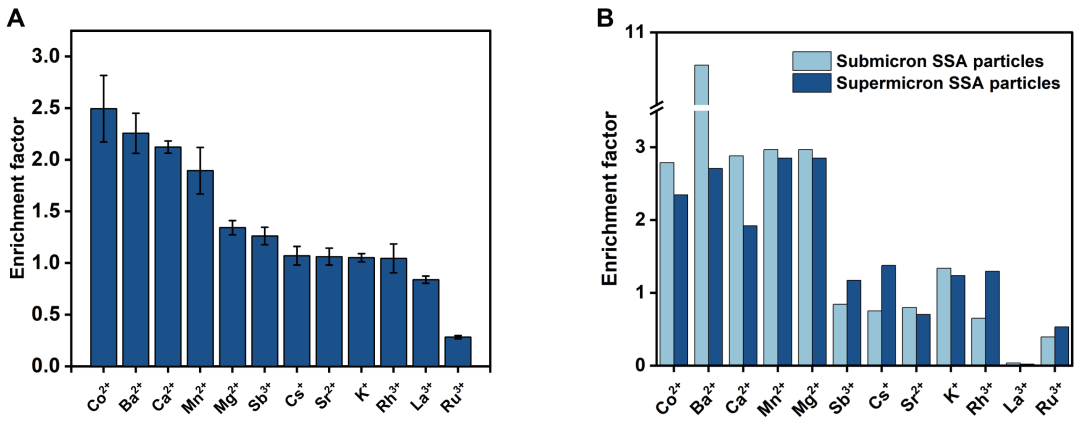


Figure 2 Enrichment factors of metal ions in full-size particle samples (A) and submicron and supermicron SSA particles (B).

facilitates the enrichment of organic matter in seawater through bridging mechanisms but its enrichment is more pronounced than those of Mg^{2+} and K^{+} [67,68]. Consequently, the enrichments of Co^{2+}, Ba^{2+}, and Mn^{2+} may also enhance the enrichment of organic matter in seawater, thereby altering visibility in the marine atmosphere and further influencing atmospheric climate over the oceans. The enrichment range of Sb^{3+}, Cs^{+}, Sr^{2+}, and Rh^{3+} falls between that of Mg^{2+} and K^{+}, indicating that these four metal ions play a role in the transfer and transport of organic matter in SSA particles similar to magnesium and potassium ions. A previous study revealed that in the 4 to 7 years following the FDNPPs accident, the concentrations of both dissolved and particulate radionuclides in river water exhibited a decreasing trend [18]. The enrichment of metal ions in SSA may be one of the major reasons for the decrease in their concentrations in water bodies. The loss of La^{3+} and Ru^{3+} in SSA particles might be due to the composition of metal ions, where the preferential enrichment of other metal ions inhibits the enrichment of these two ions.

Additionally, submicron and supermicron samples were collected to investigate the influence of particle size on the EFs of metal ions. From Figure 2B, it can be observed that the three metal ions (Co^{2+}, Ba^{2+}, and Mn^{2+}) with high overall EFs still exhibit relatively high EFs in the submicron and supermicron samples. These findings show that, similar to Ca^{2+}, they can also carry organic matter from the ocean in submicron and supermicron samples. As their EFs in the size-resolved distribution samples are higher than those in the full-size samples, the submicron and supermicron samples can transport organic matter more effectively. Similarly, it was found that the EFs of these three metal ions (Co^{2+}, Ba^{2+}, and Mn^{2+}) in submicron samples were higher than those in supermicron samples. Not only metal ions are more prone to enrichment in submicron samples, but also that their ability to carry organic matter in submicron samples may be higher than in supermicron samples. The increasing trends with decreasing particle size are similar to those found in the previous studies [69,70]. For Sb^{3+}, Cs^{+}, Sr^{2+}, and Rh^{3+}, their enrichment patterns in submicron and supermicron samples are more similar to that of K^{+}, indicating similar abilities to transport organic matter. Particularly, the EFs of Mg^{2+} in submicron and supermicron samples are both greater than those in full-size samples, which may be attributed to the minimal EFs of Mg^{2+} in samples larger than 10 μm. Additionally, except for Sr^{2+}, the EFs of the other three metal ions are higher in supermicron samples than in submicron samples. This shows that the three ions are more likely to facilitate the enrichment of organic matter in supermicron samples. Here, the EFs of the four metal ions in submicron samples are all less than 1. We

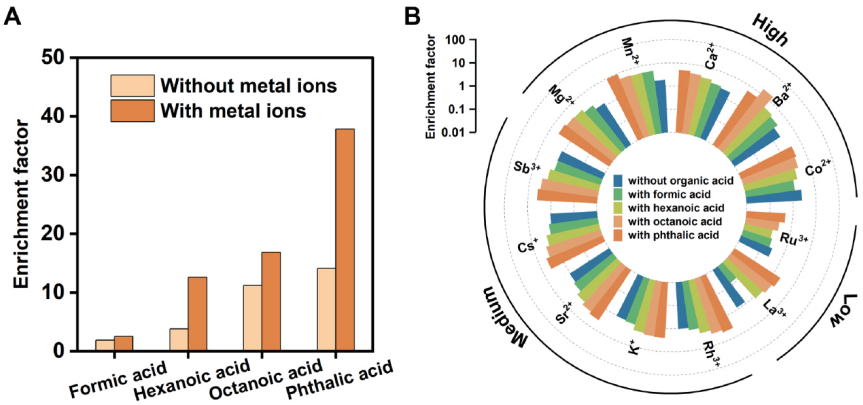


Figure 3 Enrichment factors of marine organic matter (A) and metal ions containing different marine organic matter (B) in full-size particle samples.

hypothesize that the enrichment of the negatively charged functional groups at the liquid-air interface causes metal ions to be depleted. This highlights that they are more likely to be transported through supermicron samples in the marine atmosphere. La^{3+} and Ru^{3+} exhibit the lowest EFs among all metal ions, thereby implying a lesser impact on atmospheric contamination over marine regions. Specifically, the enrichment of La^{3+} is extremely low, likely due to its greater propensity for enrichment in particles larger than 10 μm. The larger the particle size, the higher the salt concentration and the lower the organic matter concentration [36,71]. As a result, there is a propensity for La^{3+} and Ru^{3+} to remain prevalent within the marine environment, potentially due to their limited atmospheric transference and deposition. The concentration of radionuclides may have a minor impact on their EFs; however, the overall trend in enrichment remains consistent [47,69].

Interactions between marine organic matter and radionuclides

To elucidate the impact of metal ions on the translocation of marine organic matter within SSA particles, the EFs (shown in Figure 3A) of marine organic matter before and after the addition of nine metal ions were calculated. Our previous studies have shown that both the chain length and structure of organic acid molecules affect their enrichment [40,47], so we further investigated the effect of metal ions on organic acids with different chain lengths and molecular structures in this study. Following the introduction of metal ions, the EFs of marine organic matter exhibited a significant increase. Notably, the EF variations continued to adhere to the following pattern: formic acid < hexanoic acid < octanoic acid < phthalic acid. It is noteworthy that the EFs for phthalic acid and hexanoic acid are respectively more than two and three times higher than those in the samples without metal ions. These results align with our hypothesis that metal ions facilitate the enrichment of organic matter within SSA particles, thus exerting an influence on the climatic environment.

In addition, the interactions between the four above-mentioned marine organic matter and metal ions were investigated separately. For highly enriched metal ions (Co^{2+}, Ba^{2+}, and Mn^{2+}), formic acid significantly promoted the enrichment of Ba^{2+} and Mn^{2+} (Figure 3B). However, the addition of formic acid resulted in a slight decrease in Co^{2+} enrichment, indicating that Co^{2+} may inhibit the enrichment of formic acid in SSA. Based on previous studies, it is shown that formic acid has a stronger affinity for Ba^{2+} and Mn^{2+} than for Co^{2+}

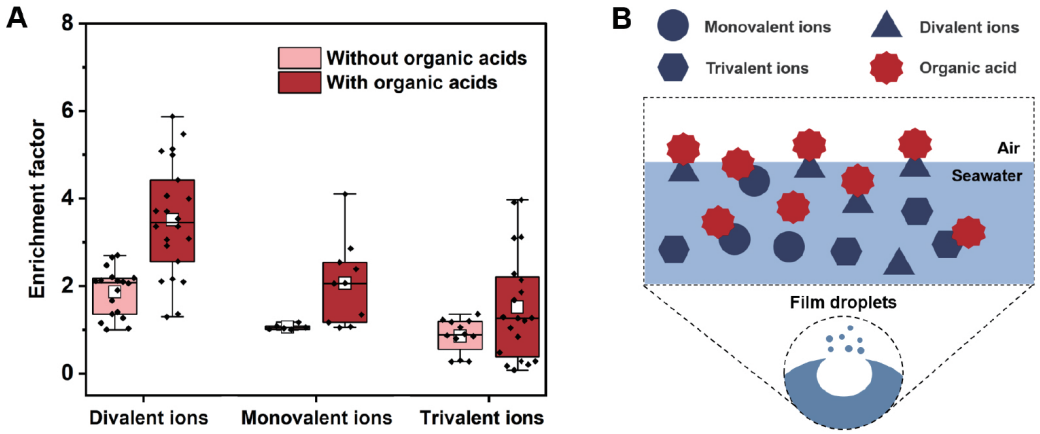


Figure 4 (A) Box-and-whisker plots of EF variations of divalent, monovalent, and trivalent ions, both with and without organic acids. The horizontal line and white dot inside the box indicate the median and mean, respectively. The vertical hinges represent data points from the lower to the upper quartile (i.e., the 25th and 75th percentiles). The whiskers represent data points from the 1st to the 99th percentile. (B) Cartoon representation of organic acids along with the metal ions within the bubble film. Divalent metal ions at the air-water interface are more efficiently transferred into the aerosol phase compared to the trivalent and monovalent metal ions present in the bulk solution away from the interface. Strong interactions between organic acids and divalent metal ions at the air-sea interface result in their greater enrichment in the resulting SSA particles.

[68,72]. This phenomenon is consistent with the enrichment of metal ions after the addition of hexanoic acid, suggesting that Co^{2+} also inhibits the enrichment of hexanoic acid in SSA. The EFs of metal ions after the addition of hexanoic acid were more significant compared to formic acid. This shows that the enrichment of hexanoic acid, which is stronger than formic acid, is also reflected in the enrichment of metal ions. The enrichment of metal ions by octanoic acid and phthalic acid demonstrated a mutually enhancing effect on the SSA particles.

For Sb^{3+}, Cs^{+}, Sr^{2+}, and Rh^{3+}, aside from the decrease in Sb^{3+} enrichment factor after the addition of formic acid, stronger enrichment effects were observed between other marine organic matter and metal ions, thereby highlighting the promoting effect of marine organic matter on the enrichment of metal ions. Furthermore, the sequence of organic acid influence on the EFs of metal ions is formic acid < hexanoic acid < octanoic acid < phthalic acid. These enrichment results suggest that in regions with abundant organic matter near the coast, the enrichment of metal ions is more pronounced, thereby exerting a greater impact on coastal residents.

Taking all the data together, divalent ions show significantly stronger enrichment than monovalent and trivalent ions. This is true regardless of whether organic acids are present in the system (Figure 4A). Furthermore, the presence of organic acids has been demonstrated to significantly promote the enrichment of metal ions, with the enrichment pattern of metal ions continuing to follow the sequence: divalent ions > monovalent ions > trivalent ions. These findings indicate that the enrichment of metal ions and organic acids occurs in the SSA particle phase, which represents the air-sea interface of a bubble. Figure 4B shows the relative distribution of metal ions and organic acids. Here organic acids are coordinated at the surface with monovalent and divalent metal ions. Trivalent metal ions are more abundant in the bulk water than at the surface and may also form complexes with other organic matter in seawater. As previously demonstrated [73–75], it can be inferred that trivalent metal ions exhibit higher apparent stability constants in comparison to divalent and monovalent metal ions. This suggests that trivalent metal ions are more prone to binding with organic ligands. However, the ability of metal ions to bind to organics does not solely rely on a single factor,

but rather on complex factors, including their charge density, hydration capacity, spatial site resistance, and even environmental conditions [76,77]. Although trivalent ions with high charge densities and stronger apparent stability constants are capable of producing strong attractive forces, they form a strong hydration layer in the solution, which results in water molecules surrounding the ions [78–82]. This makes the organics less susceptible to binding, exhibiting lower affinity for the organic ligands and inhibiting effective coordination reactions. The hydration capacity, when compared to the measured EFs in SSA particles, provides a better understanding of how selectively molecules at the air-sea interface are transferred into the SSA particle phase during the bubble-bursting process. This is likely due to a more complex and synergistic mechanism that involves interactions with metal ions present in the seawater and other species in the solution. Furthermore, interactions between organics and metal ions can only be better understood by probing the interface at a more molecular level. The measurements presented here support the need for further development of interfacial probes and a more detailed quantum chemical approach to understand the detailed interactions between the organics and metal ions.

Forward and backward trajectory simulation of air masses

Air mass trajectories describe the paths and behavior of atmospheric air masses [83–85], which can potentially carry radionuclides. The study of air mass trajectories allows us to understand the transport pathways and dispersion mechanisms of radionuclides in the atmosphere. When these air masses intersect with the marine environment, they may induce the enrichment of radionuclides. The enrichment behavior of radionuclides at the air-sea interface can be influenced by various factors, including ocean currents, climatic conditions, and solubility. Studying the trajectories of air masses can provide deeper insights into the interactions between radionuclides in the atmosphere and the ocean and their impact on the environment. Qingdao is located in eastern China, near the oceanic pathways between Japan and China. Therefore, the choice of Qingdao as a study site is aimed at gaining a better understanding of the potential impacts of Japan's radioactive waste discharge on the local environment and ecosystems. The forward trajectory simulations are designed to trace the movement of air masses containing radionuclides emitted from sources in Japan and their subsequent transport across atmospheric regions, while the backward trajectory simulations aim to identify potential source areas of radionuclides that could influence Qingdao. The simulations have been useful in determining the transport and dispersion of SSA particles containing radionuclides, thus providing greater insight into the environmental impact of Japan's discharges and the potential sources of radionuclides at Qingdao.

This study conducted both backward trajectory clustering for Qingdao, China, and forward trajectory clustering for the FDNPPs in Japan using the HYSPLIT model, respectively. The aim is to better understand the influence of radionuclides in air masses from FDNPPs, and the transport pathways of SSA particles emitted from the ocean. Due to the relatively long duration of this pollution transport, the trajectory time was set from the discharge date to April 2024 (with a duration of 7 months). The clustering results of forward trajectories in Figure 5 reveal that during this period, the airflow in Japan mainly converged toward the northeast and southwest regions, indicating that some pollutants would impact the atmospheric environment of coastal cities in China through atmospheric transport. Notably, forward air mass trajectory simulations demonstrated that radionuclides could travel significant distances via SSA particles and potentially deposit in

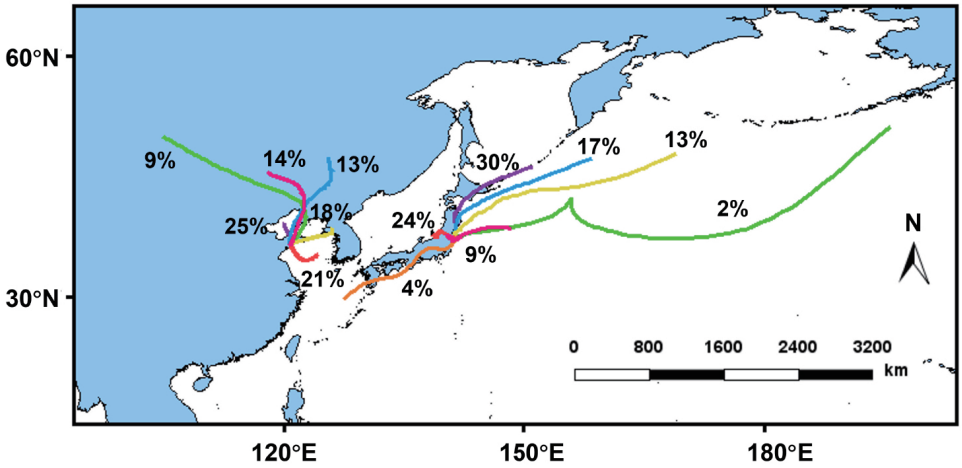


Figure 5 HYSPLIT backward trajectory clustering for Qingdao, China and forward trajectory clustering for the FDNPPs in Japan.

marine and terrestrial environments along their pathways. Such deposition has the potential to result in long-term environmental contamination, particularly in regions characterized by vulnerable ecosystems or human populations that rely on these resources. For instance, radionuclides such as Cs^{+} and Sr^{2+} have been demonstrated to accumulate in biological systems, thereby posing risks to both marine and terrestrial food chains [86–91]. The clustering results of backward trajectories showed that 39% of atmospheric pollution in Qingdao originated from long-distance transport in the northeast direction. This analysis further emphasized the dual impact of atmospheric and marine transport mechanisms on local pollution levels. To illustrate, radionuclides released into the ocean can re-enter the atmosphere as SSA particles, which are subsequently transported over long distances and contribute to additional atmospheric pollution. The regions situated along these transport pathways may potentially experience an intensification of environmental pressures, including the possibility of radiological hazards, as a consequence of the dual deposition of airborne and marine-derived pollutants [92]. The combined pollution from marine and atmospheric transport resulted in local pollution, indicating the presence of both the influence of high-altitude pollution plumes and pollution from marine emissions in the region. This emphasizes the necessity for the integrated monitoring of radionuclide transport across both atmospheric and marine pathways to mitigate their environmental and health impacts.

However, the accuracy of these transport predictions depends on the resolution and other factors involved in the trajectory simulations. The meteorological fields employed for trajectory simulations were derived from the GDAS dataset, with a spatial resolution of 1°×1° and a temporal resolution of 3 h. This resolution is adequate for capturing large-scale transport dynamics; however, finer spatial and temporal resolutions could improve the representation of mesoscale processes, such as localized wind fields, turbulence, and sea breezes, which are critical for accurately modelling transport in the marine boundary layer [93–96].

Trajectory simulations were conducted at an altitude of 100 m above ground level, a height selected to represent the transport of SSA particles within the marine boundary layer, where interactions at the air-sea interface are most active [56]. This height is appropriate for studying the behavior of SSA particles, which are predominantly formed and transported in this layer. However, variations in simulation height could influence trajectory results due to vertical changes in wind speed, direction, and turbulence, thereby introducing another source of uncertainty [43,95,97–102]. The deposition of SSA particles during transport, both dry and

wet, plays a pivotal role in determining their pathways and ultimate fate [103]. The marine boundary layer is characterized by high humidity, which enhances the hygroscopic growth of SSA particles, resulting in alterations to their size, density and deposition characteristics [100]. These physical changes exert a further influence on their transport distances and environmental impact.

To facilitate the interpretation of the extensive trajectory data, cluster analysis was employed to group similar trajectories based on spatial and temporal patterns. While this method effectively identifies principal transport pathways and reduces the complexity of the dataset, it may not fully capture the nuances of complex meteorological phenomena, especially under highly variable atmospheric conditions [104]. Consequently, biases could arise in representing localized or transient transport events. Further research should take into account resolution limitations, as well as the height of the simulation and the mechanisms of deposition, to enhance the comprehension of radionuclide transport via SSA particles and their environmental impact.

DISCUSSION

In summary, although the majority of metal ions reach the atmosphere through the ocean via SSA particles, little is known about the enrichment and interactions of these metal ions with organics. Our data suggest that surface activity and metal ions in seawater play a key role in the transfer of molecules from the air-sea interface to the film droplets produced during bubble bursting. The transfer of a significant amount of the most bridging ions, such as Ca^{2+}, during film drop formation is a consequence of non-equilibrium mixing of the bulk solution with molecules at the air-sea interface. We determined that the factors controlling the selectivity of organic and inorganic ions present in seawater are the valence of the metal ions and the surface tension of the seawater. Metal-organic complexation in seawater potentially affects the metabolic processes of organisms such as phytoplankton and marine biogeochemical cycles. This study contributes to filling existing knowledge gaps in the transfer of radionuclides from SSA particles to the atmosphere. Although the current results deepen our understanding of the transport of radionuclides, further detailed work is still needed to explore how different radionuclides affect the marine and atmospheric environments.

Data availability

The original data are available from corresponding authors upon reasonable request.

Acknowledgements

We would like to thank Nannan Dong and Jiacheng Li from State Key Laboratory of Microbial Technology of Shandong University for their help and guidance in ICP-MS.

Funding

This work was supported by the National Natural Science Foundation of China (22376121, 22361162668).

Author contributions

Y.S. did the investigation, performed experiments, analyzed the data, and wrote the manuscript. K.L., J.L., N.T.T. and L.D. provided suggestions for data analysis and manuscript writing.

Conflict of interest

The authors declare no conflict of interest.

Supplementary information

The supporting information is available online at https://doi.org/10.1360/nso/20240022. The supporting materials are published as submitted, without typesetting or editing. The responsibility for scientific accuracy and content remains entirely with the authors.

References

1 Tkalin AV, Chaykovskaya EL. Anthropogenic radionuclides in Peter the Great bay. *J Environ Radioact* 2000; **51**: 229–238.

2 Bezhin NA, Milyutin VV, Kuzmenkova NV, *et al.* Radionuclides' recovery from seawater using FIC and FIC A sorbents. *Materials* 2023; **16**: 4181.

3 Inomata Y, Aoyama M, Hirose K, *et al.* Distribution of radionuclides in surface seawater obtained by an aerial radiological survey. *J Nucl Sci Tech* 2014; **51**: 1059–1063.

4 Ito T, Aramaki T, Otosaka S, *et al.* Anthropogenic radionuclides in seawater of the japan sea. *J Nucl Sci Tech* 2005; **42**: 90–100.

5 Li R, Yan H, Wang H, *et al.* Electrodialysis for the volume reduction of the simulated radionuclides containing seawater. *J Hazard Mater* 2022; **439**: 129601.

6 Rozmaric M, Chamizo E, Louw DC, *et al.* Fate of anthropogenic radionuclides (90Sr, 137Cs, 238Pu, 239Pu, 240Pu, 241Am) in seawater in the northern Benguela upwelling system off Namibia. *Chemosphere* 2022; **286**: 131514.

7 Voronina AV, Noskova AY, Semenishchev VS, *et al.* Decontamination of seawater from 137Cs and 90Sr radionuclides using inorganic sorbents. *J Environ Radioact* 2020; **217**: 106210.

8 Aliyu AS, Evangeliou N, Mousseau TA, *et al.* An overview of current knowledge concerning the health and environmental consequences of the Fukushima Daiichi Nuclear Power Plant (FDNPP) accident. *Environ Int* 2015; **85**: 213–228.

9 Nanba K, Konoplev A, Wada T. *Behavior of Radionuclides in the Environment III*. Singapore: Springer. 2022.

10 Taniguchi K, Onda Y, Smith HG, *et al.* Dataset on the 6-year radiocesium transport in rivers near Fukushima Daiichi nuclear power plant. *Sci Data* 2020; **7**: 433.

11 Buesseler K, Dai M, Aoyama M, *et al.* Fukushima Daiichi-derived radionuclides in the ocean: Transport, fate, and impacts. *Annu Rev Mar Sci* 2017; **9**: 173–203.

12 Hirose K, Povinec PP. Ten years of investigations of Fukushima radionuclides in the environment: A review on process studies in environmental compartments. *J Environ Radioact* 2022; **251-252**: 106929.

13 Liu Y, Guo XQ, Li SW, *et al.* Discharge of treated Fukushima nuclear accident contaminated water: Macroscopic and microscopic simulations. *Natl Sci Rev* 2022; **9**: nwab209.

14 Povinec P, Hirose K, Aoyama M. *Fukushima accident: Radioactivity Impact on the Environment*. Tokyo: Elsevier, 2013.

15 Povinec P, Hirose K, Aoyama M. *Fukushima Accident: 10 Years After.* 2nd ed. Amsterdam: Elsevier, 2021.

16 Masson O, Baeza A, Bieringer J, *et al.* Tracking of airborne radionuclides from the damaged Fukushima Dai-Ichi nuclear reactors by European networks. *Environ Sci Technol* 2011; **45**: 7670–7677.

17 Steinhauser G. Fukushima's forgotten radionuclides: A review of the understudied radioactive emissions. *Environ Sci Technol* 2014; **48**: 4649–4663.

18 Nakanishi T, Sakuma K. Trend of 137Cs concentration in river water in the medium term and future following the Fukushima nuclear accident. *Chemosphere* 2019; **215**: 272–279.

19 Osanai M, Miura M, Tanaka C, *et al.* Long-term analysis of internal exposure dose-reduction effects by food regulation

and food item contribution to dose after the fukushima daiichi nuclear power plant accident. *Foods* 2023; **12**: 1305.

20 Ozawa R. Radiation measurements at Fukushima medical university over a period of 12 years following the nuclear power plant accident. *J Radiat Prot Res* 2023; **48**: 153–161.

21 Ozdemir E, Miwa S, Porcheron E, *et al.* Aerosol deposition and dispersion during nuclear reactor decommissioning. *Nucl Eng Des* 2023; **414**: 112623.

22 Sakauchi K, Otaki JM. Imaging plate autoradiography for ingested anthropogenic cesium-137 in butterfly bodies: Implications for the biological impacts of the Fukushima nuclear accident. *Life* 2023; **13**: 1211.

23 Takada M, Kuroda Y, Kanai Y, *et al.* Impacts of environmental decontamination on the rebuilding of returnees' lives after the Fukushima accident. *J Radiol Prot* 2023; **43**: 031513.

24 Teien HC, Wada T, Kashparov V, *et al.* Transfer of 129I to freshwater fish species within Fukushima and Chernobyl exclusion zones. *J Environ Radioact* 2023; **270**: 107269.

25 Tsumune D, Bryan FO, Lindsay K, *et al.* Simulated inventory and distribution of 137Cs released from multiple sources in the global ocean. *Mar Pollution Bull* 2023; **197**: 115663.

26 Yabusaki S, Asai K. Estimation of groundwater and spring water residence times near the coast of Fukushima, Japan. *Groundwater* 2023; **61**: 431–445.

27 Walling DE, Quine TA, Rowan JS. Fluvial transport and redistribution of Chernobyl fallout radionuclides. *Hydrobiologia* 1992; **235-236**: 231–246.

28 Deji, Yao T, Thompson LG, Davis ME, *et al.* Westerly drives long-distance transport of radionuclides from nuclear events to glaciers in the Third Pole. *J Environ Radioact* 2022; **255**: 107016.

29 Håkanson L. Modelling the transport of radionuclides from land to water. *J Environ Radioact* 2004; **73**: 267–287.

30 Lee HJ, Jo HY, Nam KP, *et al.* Measurement, simulation, and meteorological interpretation of medium-range transport of radionuclides to Korea during the Fukushima Dai-Ichi nuclear accident. *Ann Nucl Energy* 2017; **103**: 412–423.

31 Liu LB, Wu S, Cao JJ, *et al.* Monitoring of atmospheric radionuclides from the Fukushima nuclear accident and assessing their impact on Xi'an, China. *Chin Sci Bull* 2013; **58**: 1585–1591.

32 Mathieu A, Kajino M, Korsakissok I, *et al.* Fukushima Daiichi-derived radionuclides in the atmosphere, transport and deposition in Japan: A review. *Appl Geochem* 2018; **91**: 122–139.

33 Mori K, Tada K, Tawara Y, *et al.* Integrated watershed modeling for simulation of spatiotemporal redistribution of post-fallout radionuclides: Application in radiocesium fate and transport processes derived from the Fukushima accidents. *Environ Model Software* 2015; **72**: 126–146.

34 Otosaka S, Amano H, Ito T, *et al.* Anthropogenic radionuclides in sediment in the Japan Sea: Distribution and transport processes of particulate radionuclides. *J Environ Radioact* 2006; **91**: 128–145.

35 Semizhon T, Röllin S, Spasova Y, *et al.* Transport and distribution of artificial gamma-emitting radionuclides in the River Yenisei and its sediment. *J Environ Radioact* 2010; **101**: 385–402.

36 Freney E, Sellegri K, Nicosia A, *et al.* Mediterranean nascent sea spray organic aerosol and relationships with seawater biogeochemistry. *Atmos Chem Phys* 2021; **21**: 10625–10641.

37 Franklin EB, Amiri S, Crocker D, *et al.* Anthropogenic and biogenic contributions to the organic composition of coastal submicron sea spray aerosol. *Environ Sci Technol* 2022; **56**: 16633–16642.

38 Michaud JM, Thompson LR, Kaul D, *et al.* Taxon-specific aerosolization of bacteria and viruses in an experimental ocean-atmosphere mesocosm. *Nat Commun* 2018; **9**: 2017.

39 van Pinxteren M, Zeppenfeld S, Wadinga Fomba K, *et al.* Amino acids, carbohydrates, and lipids in the tropical oligotrophic Atlantic Ocean: Sea-to-air transfer and atmospheric *in situ* formation. *Atmos Chem Phys* 2023; **23**: 6571–6590.

40 Song Y, Li J, Tsona NT, *et al.* Enrichment of short-chain organic acids transferred to submicron sea spray aerosols. *Sci Total Environ* 2022; **851**: 158122.

41 Zinke J, Freitas G, Salter ME *et al*. Quantification and characterization of microbial emissions over the Northeastern Atlantic using mesocosm experiments. *ACS ES&T Air* 2024; **1**: 162–174.

42 Povinec PP, Sýkora I, Gera M, *et al.* Fukushima-derived radionuclides in ground-level air of Central Europe: A comparison with simulated forward and backward trajectories. *J Radioanal Nucl Chem* 2012; **295**: 1171–1176.

43 Aili A, Abuduwaili J, Xu H, *et al.* A cluster analysis of forward trajectory to identify the transport pathway of salt-dust particles from dried bottom of aral sea, central asia. *Atmosphere* 2021; **12**: 764.

44 Zhang Y, Wang N, Zhang B, *et al.* Interannual variation and chemical characterization of major water-soluble inorganic ions in snow across Northwest China. *Front Earth Sci* 2023; **11**: 1099178.

45 Auvil NC, Vazquez de Vasquez MG, Allen HC. Zinc-carboxylate binding in mixed octadecanoic acid and octadecanol monolayers on proxy seawater solution surfaces. *ACS Earth Space Chem* 2021; **5**: 2947–2956.

46 Liu L, Du L, Xu L, *et al.* Molecular size of surfactants affects their degree of enrichment in the sea spray aerosol formation. *Environ Res* 2022; **206**: 112555.

47 Song Y, Li J, Tsona Tchinda N, *et al.* Role of sea spray aerosol at the air-sea interface in transporting aromatic acids to the atmosphere. *Atmos Chem Phys* 2024; **24**: 5847–5862.

48 Xu M, Tsona Tchinda N, Li J, *et al.* Insoluble lipid film mediates transfer of soluble saccharides from the sea to the atmosphere: The role of hydrogen bonding. *Atmos Chem Phys* 2023; **23**: 2235–2249.

49 Quinn PK, Coffman DJ, Johnson JE, *et al.* Small fraction of marine cloud condensation nuclei made up of sea spray aerosol. *Nat Geosci* 2017; **10**: 674–679.

50 Xu W, Ovadnevaite J, Fossum KN, *et al.* Sea spray as an obscured source for marine cloud nuclei. *Nat Geosci* 2022; **15**: 282–286.

51 Sha B, Johansson JH, Tunved P, *et al.* Sea spray aerosol (SSA) as a source of perfluoroalkyl acids (PFAAs) to the atmosphere: field evidence from long-term air monitoring. *Environ Sci Technol* 2021; **56**: 228–238.

52 Hernandez-Jaramillo DC, Harrison L, Kelaher B, *et al.* Evaporative cooling does not prevent vertical dispersion of effervescent seawater aerosol for brightening clouds. *Environ Sci Technol* 2023; **57**: 20559–20570.

53 Lenain L, Melville WK. Evidence of sea-state dependence of aerosol concentration in the marine atmospheric boundary layer. *J Phys Oceanogr* 2017; **47**: 69–84.

54 Crawford J, Cohen DD, Chambers SD, *et al.* Impact of aerosols of sea salt origin in a coastal basin: Sydney, Australia. *Atmos Environ* 2019; **207**: 52–62.

55 Parameswaran K. Influence of micrometeorological features on coastal boundary layer aerosol characteristics at the tropical station, Trivandrum. *J Earth Syst Sci* 2001; **110**: 247–265.

56 Porter JN, Lienert BR, Sharma SK, *et al.* Vertical and horizontal aerosol scattering fields over Bellows Beach, Oahu, during the SEAS experiment. *J Atmos Ocean Technol* 2003; **20**: 1375–1387.

57 Liu S, Liu CC, Froyd KD, *et al.* Sea spray aerosol concentration modulated by sea surface temperature. *Proc Natl Acad Sci USA* 2021; **118**: e2020583118.

58 Zhu C, He Q, Zhao Z, *et al.* Comparative analysis of ozone pollution characteristics between urban area and southern mountainous area of urumqi, china. *Atmosphere* 2023; **14**: 1387.

59 Wang YQ. MeteoInfo: GIS software for meteorological data visualization and analysis. *Met Apps* 2014; **21**: 360–368.

60 Huang X, Chen Y, Meng Y, *et al.* Mitigating airborne microplastics pollution from perspectives of precipitation and underlying surface types. *Water Res* 2023; **243**: 120385.

61 Wang YQ, Zhang XY, Draxler RR. TrajStat: GIS-based software that uses various trajectory statistical analysis methods to identify potential sources from long-term air pollution measurement data. *Environ Model Software* 2009; **24**: 938–939.

62 Saliba G, Chen CL, Lewis S, *et al.* Factors driving the seasonal and hourly variability of sea-spray aerosol number in the North Atlantic. *Proc Natl Acad Sci USA* 2019; **116**: 20309–20314.

63 Guzmán E, Santini E, Benedetti A, *et al.* Surfactant induced complex formation and their effects on the interfacial properties of seawater. *Colloids Surfs B-Biointerfaces* 2014; **123**: 701–709.

64 Hamidian R, Lashkarbolooki M, Amani H. Ion type adjustment with emphasize on the presence of NaCl existence; measuring interfacial tension, wettability and spreading of crude oil in the carbonate reservoir. *J Pet Sci Eng* 2019; **182**:

106266.

65 Ramezani M, Lashkarbolooki M, Abedini R, *et al.* Role of salinity concomitant with asphaltene and resin on the interfacial tension of ionic liquid from imidazolium family. *J Pet Sci Eng* 2022; **219**: 111117.

66 Steffens SD, Cook EK, Sedlak DL, *et al.* Under-reporting potential of perfluorooctanesulfonic acid (PFOS) under high-ionic strength conditions. *Environ Sci Technol Lett* 2021; **8**: 1032–1037.

67 Adams EM, Allen HC. Palmitic acid on salt subphases and in mixed monolayers of cerebrosides: application to atmospheric aerosol chemistry. *Atmosphere* 2013; **4**: 315–336.

68 Cochran RE, Jayarathne T, Stone EA, *et al.* Selectivity across the interface: A test of surface activity in the composition of organic-enriched aerosols from bubble bursting. *J Phys Chem Lett* 2016; **7**: 1692–1696.

69 Sha B, Johansson JH, Benskin JP, *et al.* Influence of water concentrations of perfluoroalkyl acids (PFAAS) on their size-resolved enrichment in nascent sea spray aerosols. *Environ Sci Technol* 2021; **55**: 9489–9497.

70 Triesch N, van Pinxteren M, Salter M, *et al.* Sea spray aerosol chamber study on selective transfer and enrichment of free and combined amino acids. *ACS Earth Space Chem* 2021; **5**: 1564–1574.

71 Cravigan LT, Mallet MD, Vaattovaara P, *et al.* Sea spray aerosol organic enrichment, water uptake and surface tension effects. *Atmos Chem Phys* 2020; **20**: 7955–7977.

72 Shaloski MA, Sobyra TB, Nathanson GM. DCl transport through dodecyl sulfate films on salty glycerol: Effects of seawater ions on gas entry. *J Phys Chem A* 2015; **119**: 12357–12366.

73 Gabriel JL, Aogaichi T, Dearolf CR, *et al.* Apparent stability constants of magnesium and calcium complexes of tricarboxylates. *Anal Lett* 2006; **16**: 113–127.

74 Song Y, Li T, Zhang X, *et al.* Effect of different valence metal ions on rice protein fibrillation: Binding mechanism, structural characterization and rheology. *Food Biophys* 2023; **18**: 570–579.

75 Karavoltsos S, Sakellari A, Plavšić M, *et al.* Metal complexation, FT-IR characterization, and plankton abundance in the marine surface microlayer of coastal areas in the Eastern Mediterranean. *Front Mar Sci* 2022; **9**: 932446.

76 Chang CM, Wang MK. Linear relationship for acidity and stability in hexaaqua metal ions-density functional studies. *Chem Phys Lett* 1998; **286**: 46–50.

77 El-Dossoki FI, Mohamed AAAEW. Thermodynamic parameters of phenylglycine interaction with UO_2^{2+}, La^{3+} and Zr^{4+}. *BMC Chem* 2023; **17**: 57.

78 Arulsamy AD. Correlation between ionization and hydration energies. *J Solution Chem* 2024; **53**: 1633–1650.

79 Canaval LR, Rode BM. The hydration properties of Eu(II) and Eu(III): An *ab initio* quantum mechanical molecular dynamics study. *Chem Phys Lett* 2015; **618**: 78–82.

80 Lee CL, Hsi HC, Chang CM. Linear correlation between electronegativity and adsorption energy of hydrated metal ions by carboxyl-functionalized single-walled carbon nanotubes. *J Nanopart Res* 2023; **25**: 59.

81 Marques MA, Caba$ccedil$o MI, Marques MIB, *et al.* Intermediate-range order in aqueous solutions of salts constituted of divalent ions combined with monovalent counter-ions. *J Phys-Condens Matter* 2002; **14**: 7427–7448.

82 Persson I. Structure and size of complete hydration shells of metal ions and inorganic anions in aqueous solution. *Dalton Trans* 2024; **53**: 15517–15538.

83 Pérez IA, Artuso F, Mahmud M, *et al.* Applications of air mass trajectories. *Adv Meteor* 2015; **2015**: 1–20.

84 Mukhtarov R, Ibragimova OP, Omarova A, *et al.* An episode-based assessment for the adverse effects of air mass trajectories on PM2.5 levels in Astana and Almaty, Kazakhstan. *Urban Clim* 2023; **49**: 101541.

85 Godłowska J, Hajto MJ, Tomaszewska AM. Spatial analysis of air masses backward trajectories in order to identify distant sources of fine particulate matter emission / Analiza przestrzenna wstecznych trajektorii mas powietrza w celu rozpoznania odległych źródeł emisji pyłu drobnego. *Arch Environ Prot* 2015; **41**: 28–35.

86 Bok-Badura J, Jakóbik-Kolon A. Cesium ion sorption on hybrid pectin-Prussian blue beads: Batch and column studies to remove radioactive cesium from contaminated wastewater. *Hydrometallurgy* 2022; **213**: 105937.

87 Hong HJ, Park IS, Ryu T, *et al.* Demonstration of seawater strontium (Sr(II)) extraction and enrichment by a biosorption technique through continuous column operation. *Ind Eng Chem Res* 2018; **57**: 12909–12915.

88 Kameník J, Dulaiova H, Šebesta F, *et al.* Fast concentration of dissolved forms of cesium radioisotopes from large seawater samples. *J Radioanal Nucl Chem* 2013; **296**: 841–846.

89 Ferrier-Pagès C, Boisson F, Allemand D, *et al.* Kinetics of strontium uptake in the scleractinian coral Stylophora pistillata. *Mar Ecol Prog Ser* 2002; **245**: 93–100.

90 Bouchalkha A, Karli R, Alhammadi K. Reusable sensor for strontium sulfate scale monitoring in seawater. *Materials* 2021; **14**: 676.

91 Zhu L, Hou X, Qiao J. Determination of low-level 135Cs and 135Cs/137Cs atomic ratios in large volume of seawater by chemical separation coupled with triple-quadrupole inductively coupled plasma mass spectrometry measurement for its oceanographic applications. *Talanta* 2021; **226**: 122121.

92 Marginson H, MacMillan GA, Wauthy M, *et al.* Drivers of rare earth elements (REEs) and radionuclides in changing subarctic (Nunavik, Canada) surface waters near a mining project. *J Hazard Mater* 2024; **471**: 134418.

93 Xia X, Chen H, Zhang W. Analysis of the dependence of column-integrated aerosol properties on long-range transport of air masses in Beijing. *Atmos Environ* 2007; **41**: 7739–7750.

94 Anastassopoulos A. An assessment of meteorological effects on air quality in Windsor, Ontario, Canada — sensitivity to temporal modeling resolution. *J Env Inform* 2008; **11**: 45–50.

95 Tošić I, Unkašević M. Extreme daily precipitation in Belgrade and their links with the prevailing directions of the air trajectories. *Theor Appl Climatol* 2013; **111**: 97–107.

96 Koracin D, Vellore R, Lowenthal DH, *et al.* Regional source identification using lagrangian stochastic particle dispersion and hysplit backward-trajectory models. *J Air Waste Manage Assoc* 2011; **61**: 660–672.

97 Shi S, Cheng T, Gu X, *et al.* Biomass burning aerosol characteristics for different vegetation types in different aging periods. *Environ Int* 2019; **126**: 504–511.

98 Escudero M, Stein A, Draxler RR, *et al.* Determination of the contribution of northern Africa dust source areas to PM10 concentrations over the central Iberian Peninsula using the Hybrid Single-Particle Lagrangian Integrated Trajectory model (HYSPLIT) model. *J Geophys Res* 2006; **111**: D06210.

99 Lee S, Ashbaugh L. The impact of trajectory starting heights on the MURA trajectory source apportionment (TSA) method. *Atmos Environ* 2007; **41**: 7022–7036.

100 Zhan MJ, Sun JY, Yin JM. Influence of air masses on particle number concentration and size distribution at Mt. Waliguan, Qinghai Province, China. *Sci Cold Arid Reg* 2011; **3**: 436–440.

101 Zhou X, Wu L, Liu Q, *et al.* Influence of low-level, high-entropy air in the eye on tropical cyclone intensity: A trajectory analysis. *J Meteorol Soc Jpn* 2020; **98**: 1231–1243.

102 Liuzzi V, Della Corte V, Rotundi A, *et al.* Zero-pressure balloons trajectory prediction: Duster flight simulations. *Adv Space Res* 2020; **66**: 1876–1886.

103 Chai T, Draxler R, Stein A. Source term estimation using air concentration measurements and a Lagrangian dispersion model – Experiments with pseudo and real cesium-137 observations from the Fukushima nuclear accident. *Atmos Environ* 2015; **106**: 241–251.

104 Yang L, Sun L, Wang D, *et al.* Analysis of precipitable water vapour characteristics from GNSS measurements during the snow season in Liaoning Province, China. *Adv Space Res* 2021; **67**: 2347–2358.